

Wavelet Denoising of High-Bandwidth Nanopore and Ion-Channel Signals

Siddharth Shekar,[†] Chen-Chi Chien,[§] Andreas Hartel,[†] Peijie Ong,[‡] Oliver B. Clarke,^{||} Andrew Marks,^{||} Marija Drndic,[§] and Kenneth L. Shepard^{*,†}

[†]Department of Electrical Engineering and [‡]Department of Applied Physics and Applied Mathematics, Columbia University, New York, New York 10027, United States

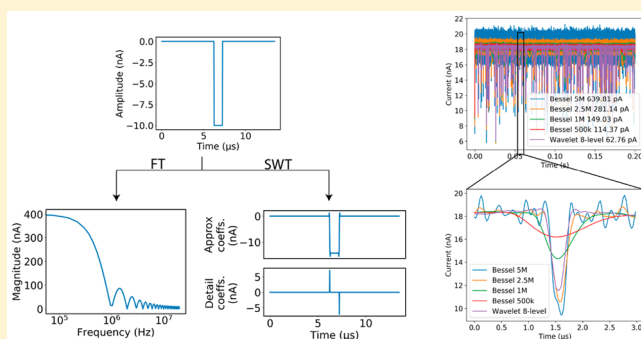
[§]Department of Physics and Astronomy, University of Pennsylvania, Philadelphia, Pennsylvania 19104, United States

^{||}Department of Physiology and Cellular Biophysics, Columbia University, New York, New York 10032, United States

S Supporting Information

ABSTRACT: Recent work has pushed the noise-limited bandwidths of solid-state nanopore conductance recordings to more than 5 MHz and of ion channel conductance recordings to more than 500 kHz through the use of integrated complementary metal-oxide-semiconductor (CMOS) integrated circuits. Despite the spectral spread of the pulse-like signals that characterize these recordings when a sinusoidal basis is employed, Bessel filters are commonly used to denoise these signals to acceptable signal-to-noise ratios (SNRs) at the cost of losing many of the faster temporal features. Here, we report improvements to the SNR that can be achieved using wavelet denoising instead of Bessel filtering. When combined with state-of-the-art high-bandwidth CMOS recording instrumentation, we can reduce baseline noise levels by over a factor of 4 compared to a 2.5 MHz Bessel filter while retaining transient properties in the signal comparable to this filter bandwidth. Similarly, for ion-channel recordings, we achieve a temporal response better than a 100 kHz Bessel filter with a noise level comparable to that achievable with a 25 kHz Bessel filter. Improvements in SNR can be used to achieve robust statistical analyses of these recordings, which may provide important insights into nanopore translocation dynamics and mechanisms of ion-channel function.

KEYWORDS: Nanopore, ion channel, wavelet, CMOS, SNR, denoise



Ion-channel proteins are responsible for regulating the cellular concentrations of ions by virtue of their ion selectivity and gating behavior. Ionic fluxes regulate key cellular functions such as muscle contraction, hormone and neurotransmitter release, and the growth and death of cells, rendering these proteins important pharmaceutical targets.^{1,2} Physiological studies focused on the functional behavior of single ion channels typically involve measuring the transmembrane current in response to electrical or chemical stimuli.² The observed gating behavior and its associated temporal dynamics provide insights as to the structure and function of ion channels.

Nanopores, analogs of leak ion channels, are nanometer-sized openings created in a thin membrane. Depending on the nature of the membrane, nanopores are either biological or solid-state.^{3–5} While not generally gateable, the temporal dynamics of the translocation of biopolymeric molecules through these pores in response to electrical gradients are similar to those exhibited by gated channels. Translocation of a molecule through the pore transiently blocks ionic conduction, and the resulting current blockage can then be used to study transport velocity,^{6,7} effective molecular charge,^{8,9} polymer lengths,¹⁰ and the molecule's

conformation^{11–13} during translocation. Significant work over the past few years has been directed toward the fabrication of solid-state nanopores with dimensions comparable to those of biological ion channels,^{14–16} which have been applied to the detection of many different analytes.^{11,13,17–20}

The front-end measurement circuitry for recording signals with both ion channels and nanopores consists primarily of a transimpedance amplifier (TIA). The sensor in either case can be modeled as a resistor in parallel with a capacitor and a current source as shown in Figure 1a. While improving the temporal resolution of these recordings is desirable for many reasons, several sources of noise (Figure 1b) limit the available SNR at any given frequency, where $SNR = \Delta I / I_{RMS}$ with ΔI being the amplitude of the pulse-like signal and I_{RMS} being the standard deviation of the baseline noise in the time trace. At low frequencies, flicker noise from the measurement electronics and the channel/pore leads to a $1/f$ characteristic in the power

Received: October 31, 2018

Revised: December 10, 2018

Published: January 2, 2019

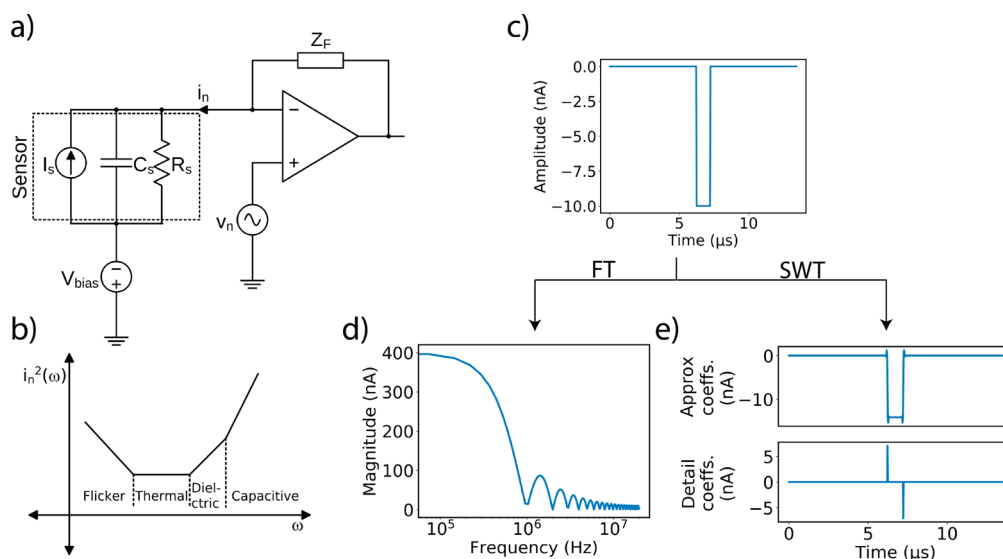


Figure 1. Typical measurement setups for nanopore and ion-channel recordings. (a) Equivalent circuit representation of a nanopore/ion channel sensor and the front-end amplifier circuitry for recording from these sensors. (b) Input-referred noise spectral density with the various dominant noise sources as a function of frequency in these systems. (c) Idealized input signal and its transformations using (d) the Fourier transform (FT) and (e) the stationary wavelet transform (SWT). Compared to the FT, the SWT offers a sparser representation of the input signal.

spectral density.^{21,22} The noise in the mid frequencies is spectrally white and is dominated by thermal and shot noise from the channel/pore,^{22–24} whereas the high-frequency noise is dominated by loss mechanisms in the membrane dielectric that increase linearly with frequency, and the amplifier's input-referred voltage noise v_n interacting with the total capacitance ΣC_i at the amplifier's input, which appears with an f^2 dependence on frequency.^{22,24} Assuming that ΔI is large enough to yield sufficient SNR to operate in the high-frequency regime and the noise is dominated by the measurement electronics (which characterizes the experimental conditions considered here), the maximum available bandwidth is governed by:

$B_{\max} \propto \left(\frac{\Delta I}{v_n \Sigma C_i} \right)^{2/3}$. Several efforts have shown ways of improving the SNR and, consequently, B_{\max} through careful design of the front-end amplifier²⁵ and through tight integration of sensor and custom-designed complementary metal-oxide-semiconductor (CMOS) electronics in the context of both ion channels and solid-state nanopores.^{19,20,26–30}

A standard technique for improving SNR after measurement is to low-pass filter the data, sacrificing bandwidth and, therefore, temporal resolution in the signal to reduce noise. Bessel filters are generally employed for this purpose because of their uniform group delay characteristics.³¹ In addition to Bessel filters, other denoising approaches that rely on hidden Markov models (HMMs) have been applied to both nanopore^{32,33} and ion-channel recordings.^{34–36} However, these techniques require assumptions to be made about the underlying model and are, in general, more computationally expensive than the denoising technique explored here. This computational complexity further increases in the context of signals corrupted by f^2 noise, where “meta-states” may need to be introduced to deal with the correlation between noise in adjacent data points.³⁵

In this Letter, we report on SNR improvements that can be attained by applying a wavelet denoising technique to high-bandwidth conductance data obtained using integrated CMOS electronics, which represent the fastest such recordings to date.^{19,30} Wavelet transform and denoising of time-series data

has been explored in a wide variety of contexts.^{37–41} While there has been some prior work applying wavelet denoising techniques to data from ensemble ion channels,⁴² Coulter counter,⁴³ and nanopores,⁴⁴ the intrinsic SNR available in these studies has been relatively low due to the absence of electronics optimized for high-bandwidth measurements.

Figure 1c shows an idealized representative noise-less pulse. Because the Fourier transform uses sinusoids that exist for all time as its basis functions, the representation of a short-lived pulse in such a basis is not sparse (Figure 1d). As a result, a low-pass filter designed in the frequency domain used to improve SNR by reducing noise levels will result in a smoothed version of the signal in the time domain. In contrast, the wavelet transform (Figure 1e) yields a set of approximation and detail coefficients at each level of decomposition that correspond approximately to the low- and high-frequency components of the signal, respectively, at that level.⁴⁵ The result is a much sparser representation of the signal that allows more-aggressive filtering of the noise, which is spread out across coefficients, to be performed without significantly affecting the time-domain characteristics of the signal.

In the wavelet transform, the coefficients at a given level are obtained by convolving the approximation coefficients of the previous level (or the signal itself at the first level) with the scaling and wavelet functions and their translated versions. Changing the level of decomposition is achieved by changing the dilation factor for these functions. Specifically, in the denoising that we present here, we consider only the dyadic case in which the dilation factor is two and translations are only by integer amounts. The sparsity in the coefficients obtained using the wavelet transform is due to the compact support of the wavelets employed (in our case, the biorthogonal wavelet^{46,47} 1.5; see the Supporting Information).

The wavelet transform has been the focus of extensive work and is commonly used in image compression algorithms.^{45,48} The most-common version of the wavelet transform, called the discrete wavelet transform (DWT), decimates the wavelet coefficients by a factor of 2 at each decomposition level. This results in a non-redundant representation of the signal, such that

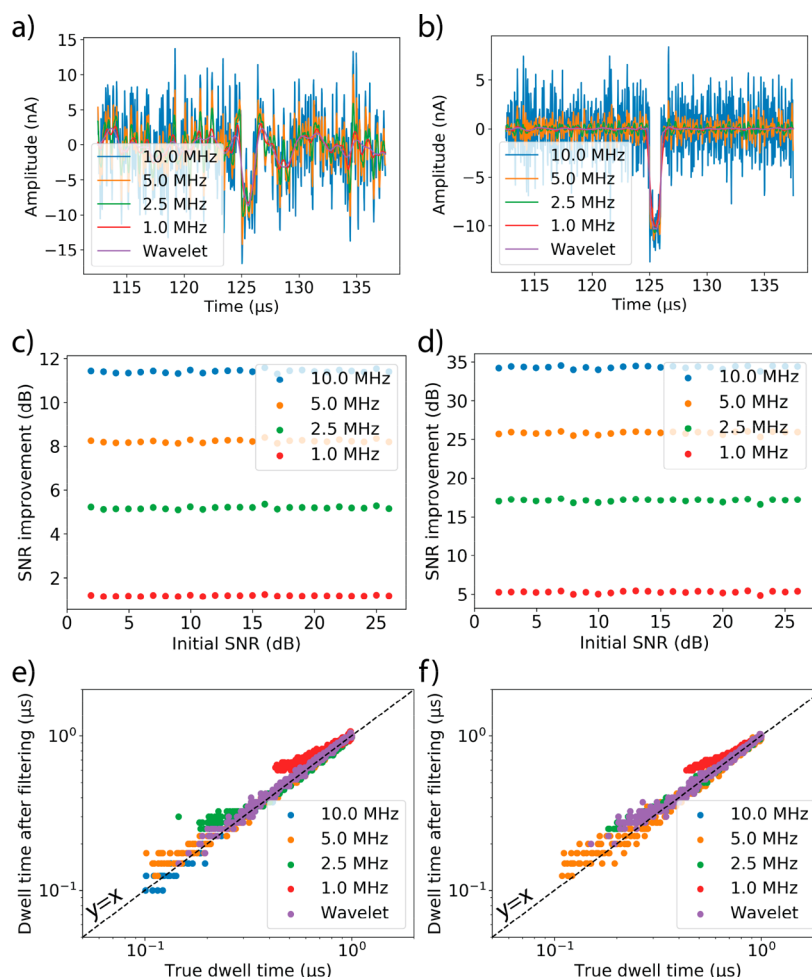


Figure 2. Performance comparison of wavelet denoising (5-level, LDT, garrote) vs standard Bessel filters for simulated noisy pulses. The data are generated at 40 MSPS with a baseline of 0 and an amplitude of -10 nA. (a) Representative time trace of a $1 \mu\text{s}$ long pulse corrupted by white noise at the worst-case initial SNR of ~ 2 dB filtered by 1, 2.5, 5, and 10 MHz fourth-order Bessel filters and wavelet denoising. (c) For the same pulse width of $1 \mu\text{s}$ and corruption by white noise to a range of initial SNR values, wavelet denoising offers consistent reductions in baseline noise levels (averaged over 100 repetitions) compared with 1, 2.5, 5, and 10 MHz fourth-order Bessel filters. Because the amplitude of the signal remains unchanged in all of these cases, this directly translates to an improved SNR. (e) For 500 simulated pulses with widths ranging from 0.1 to $1 \mu\text{s}$ and an initial SNR of 14 dB, wavelet denoising retains the pulse width information better than both the 1 and the 2.5 MHz filters. Panels b, d, and f are the same as panels a, c, and e except for the noise source, which is f^2 instead of white. Here, wavelet denoising offers increased improvement in SNR and has shape retention similar to that of the 2.5 MHz filter.

a signal of length N yields N corresponding wavelet coefficients. However, this transformation is not translation-invariant, which can create artifacts during reconstruction after denoising.⁴⁹ As a result, the studies here instead employ the stationary wavelet transform (SWT), which yields a redundant representation of the signal, giving N detail coefficients per level of decomposition and N approximation coefficients at level J for a total of $N(J+1)$ wavelet coefficients for J levels of decomposition. Denoising⁵⁰ using the wavelet transform consists of the following steps:

1. choose a wavelet basis;
2. choose the maximum decomposition level J ;
3. compute the wavelet transform for the signal $x[n]$ to obtain detail coefficients $w_{j,k}$ and approximation coefficients $a_{J,k}$, where $j = 1, \dots, J$ and $k = 1, \dots, N_j$;
4. calculate the noise threshold λ_j for $w_{j,k}$;
5. choose a thresholding scheme T and threshold $w_{j,k}$ to obtain $w'_{j,k} = T(w_{j,k})$; and
6. perform the inverse wavelet transform using $a_{J,k}$ and $w'_{j,k}$.

For good denoising, the wavelet basis must be chosen so as to concentrate the signal information in a few high-valued coefficients while the noise is spread uniformly over coefficients. For this study, we used the biorthogonal 1.5 wavelet (see the [Supporting Information](#) for details). Higher values of J lead to increased noise reduction at the expense of potentially greater smoothing of the signal. The root-mean-square (RMS) noise level σ_j of the detail coefficients can either be estimated by using the median absolute deviation (MAD) as $\sigma_j = \frac{\text{median}(|w_{j,k} - \text{mean}(w_{j,k})|)}{0.6745}$ or, if available, can be directly calculated from the wavelet transform of pure-noise data. Several schemes exist to calculate λ_j once σ_j is known, such as the universal threshold,⁵⁰ level-dependent threshold (LDT),⁵¹ Stein's unbiased risk estimate (SURE),⁵² minimax threshold,⁵⁰ or Bayesian threshold.⁵³ Of these, we employ the LDT due to its simplicity and robustness. The LDT is calculated as $\lambda_j = \sigma_j \sqrt{2 \ln(N_j)}$ where N_j is the number of detail coefficients $w_{j,k}$ at decomposition level j , and is N in the case of the SWT.

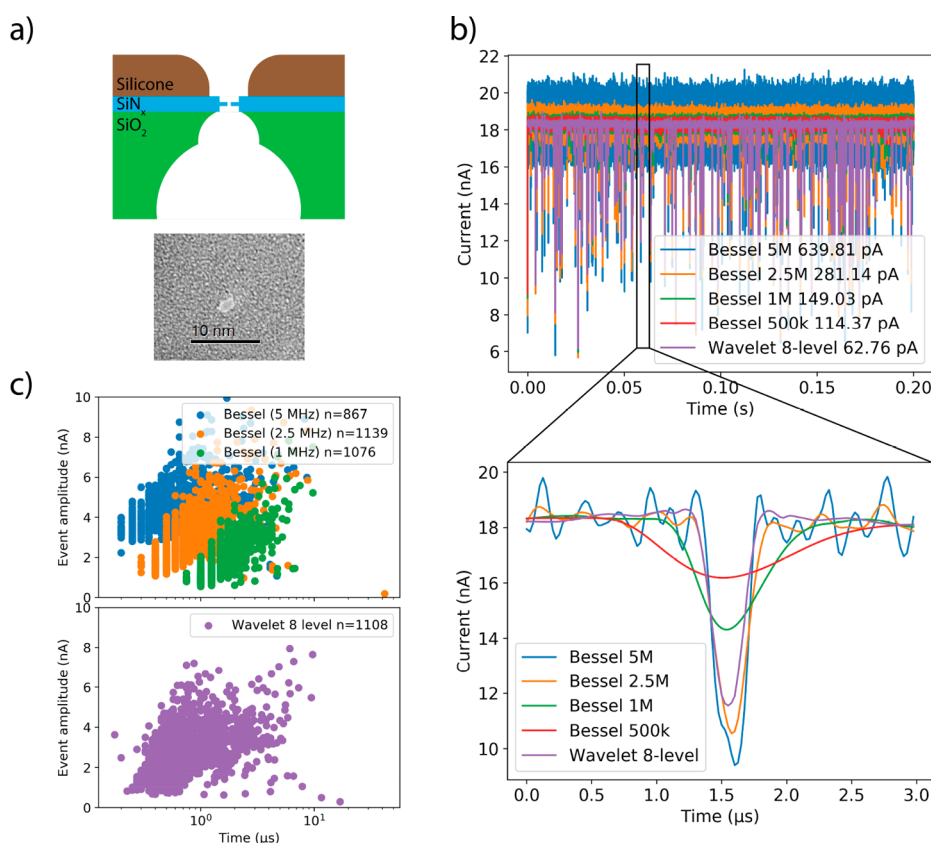


Figure 3. Denoising of high-bandwidth solid-state nanopore recordings. The data were obtained using a system with an acquisition rate of 40 MSPS and a hardware fourth-order Bessel filter at 10 MHz. (a) Schematic of the cross-section of the glass-passivated nanopore (not to scale) and TEM image of the 1.2 nm × 1.7 nm diameter nanopore used in this study. (b) Time trace of 90-nucleotide-long ssDNA translocation through the nanopore in 3 M KCl at 700 mV bias. The same signal segment is filtered to different bandwidths using Bessel filters implemented in software vs eight-level SWT denoising with LDT and garrote thresholding. The numbers in the legend indicate the noise level (in pA_{RMS}) calculated over a 1 ms window. The expanded time trace of a single event shows that wavelet denoising offers shape retention better than the 1 MHz filter and comparable to that of the 2.5 MHz filter. (c) Amplitude vs dwell-time histogram showing that the wavelet denoised trace statistically offers nearly identical performance compared to the 2.5 MHz filter with <4 times the baseline noise level. Events here were identified as having a minimum deviation of 8σ from the baseline.

Choosing the right threshold plays a critical role in the trade-off between the denoising and smoothing of the signal. Once λ_j has been determined, several options exist for the choice of T , such as the classical hard and soft,⁵⁰ firm,⁵⁴ non-negative garrote,⁵⁵ and others^{56,57} (see the [Supporting Information](#) for details). In general, hard thresholding preserves edge sharpness better but can suffer from artifacts caused by noise coefficients slightly larger than the threshold being preserved unaltered. On the other hand, soft thresholding is more immune to these artifacts but provides greater smoothing of the signal. For the nanopore data, we used the garrote thresholding scheme given by:

$$T(x, \lambda) = \begin{cases} 0 & \text{if } |x| \leq \lambda \\ x - \frac{\lambda^2}{x} & \text{if } |x| > \lambda \end{cases}$$

Garrote thresholding offers a good compromise between hard and soft thresholding by providing good noise immunity for coefficient values close to λ while leaving the large-valued coefficients largely untouched. For the ion channel data, we observed that the garrote thresholding method behaves almost identically to the soft thresholding method. As a result, we used hard thresholding that yields sharper rising and falling edges without significantly increasing noise levels. We implemented all

of our wavelet signal processing in Python using the PyWavelets module.

We tested the wavelet denoising method first on simulated data with either of two spectrally distinct kinds of noise added to it: white or f^2 (see the [Supporting Information](#) for details). The latter is particularly relevant for high-bandwidth current measurements using a TIA-like front-end.²⁴ The wavelet denoising schemes evaluated in this work assume that the detail coefficients obey a Gaussian amplitude distribution. Strong noise components at individual frequencies, as is the case with electromagnetic interference, could violate this assumption and lead to ineffective denoising performance. In general, the effect of such noise sources can be mitigated during the measurement by shielding. We simulated the data assuming a sampling rate of 40 MSPS and padded the pulse with 5000 points on each side. Representative 1 μs pulses are shown in [Figure 2a,b](#) at the worst-case initial SNR of ~2 dB processed by fourth-order Bessel filters with cutoff frequencies at 1, 2.5, 5, and 10 MHz and by wavelet denoising. We note that while we treat the simulated signal to be a current waveform, wavelet denoising can be applied to other signals with similar temporal characteristics.

Panels c and d of [Figure 2](#) show the SNR improvement offered by wavelet denoising compared with the Bessel filters over a range of initial SNR values. This is necessary because, unlike the Bessel filters, wavelet denoising is a nonlinear technique and its

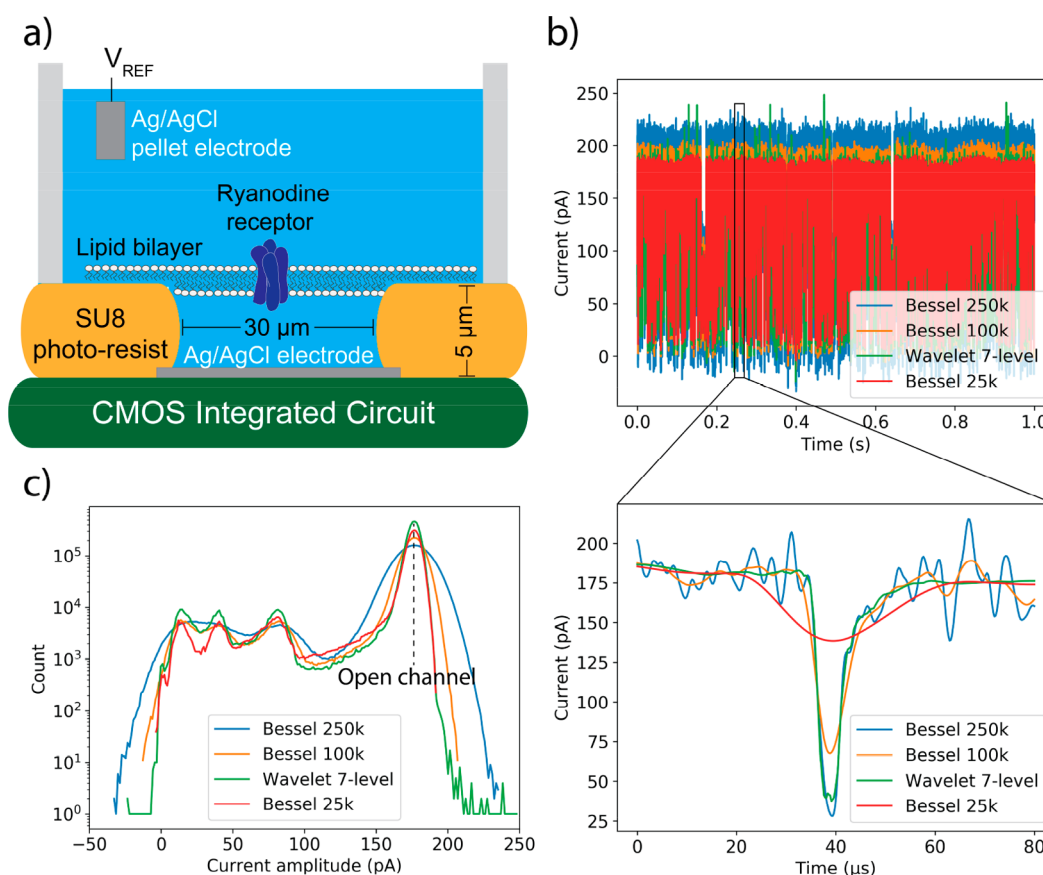


Figure 4. Denoising of high-bandwidth ion-channel recordings. The data were obtained using a system measuring RyR1 activity at 200 mV bias in 1 M KCl with 1 mM ATP. The measurement system has an acquisition rate of 40 MSPS and a hardware fourth-order Bessel filter at 10 MHz. The data are then filtered using a 1 MHz fourth-order Bessel filter and downsampled to 4 MSPS. (a) Schematic of the ion-channel measurement apparatus. A single RyR1 channel is incorporated into a suspended lipid bilayer created on an SU-8 well fabricated directly on top of the CMOS amplifier chip. (b) Time-trace of the same signal segment filtered to different bandwidths using Bessel filters implemented in software vs seven-level SWT denoising with hard thresholding using LDT thresholds extracted from noisy data. The upward spikes in the wavelet denoised trace are artifacts created by the hard thresholding scheme and are infrequent enough to not significantly affect statistical performance. The expanded trace of a single event shows that wavelet denoising offers shape retention better than that of the 100 kHz filter and significantly better than the 25 kHz filter. (c) All-points amplitude histogram with the Y axis showing the bin count on a logarithmic scale. Wavelet denoising has noise performance comparable to that of the 25 kHz filter, as shown by the width of the peak near the open channel current.

performance is dependent on the signal amplitude relative to that of the noise. When averaged over 100 simulations for both white and f^2 noise, five-level SWT denoising with LDT and garrote thresholding offers SNR improvement compared with all of the Bessel filters tested here. These improvements in noise performance also persist over a range of initial SNR values.

Panels e and f of Figure 2 show that wavelet denoising offers good signal-shape retention compared to the same set of fourth-order Bessel filters, when the initial pulse width is varied from 100 ns to 1 μs. The dwell time here is calculated as the full-width-at-half-maximum. For a denoising scheme that does not result in any signal distortion, the scatter plot would be along the straight line $y = x$. With white noise, the dwell time performance of wavelet denoising is better than that of the 2.5 MHz Bessel filter, whereas with f^2 noise, the two perform similarly. This temporal performance is achieved with a simultaneous SNR improvement of 5.5 and 17 dB (Figure 2c,d) when the noise shape is white and f^2 , respectively. In scenarios with multiple events, spacing between events does not strongly affect the performance of wavelet denoising (see the Supporting Information for details).

Given the improvements that wavelet denoising can offer in a simulated context, we applied this technique to high-bandwidth

nanopore recordings. These data are obtained using an integrated CMOS transimpedance amplifier described elsewhere.¹⁹ We packaged the amplifier with glass-passivated⁵⁸ ultrathin¹⁶ nanopores to measure translocations of 90-nucleotide ssDNA in 3 M KCl. This combination of tightly integrated custom amplifiers and low-capacitance nanopore membranes allows us to achieve SNRs of better than six at 10 MHz bandwidth. The signals presented here were obtained using a 1.2 nm × 1.7 nm pore (Figure 3a) at 700 mV of applied bias (see the Supporting Information for details). Figure 3b plots a 200 ms time trace comparing the raw data filtered by fourth-order Bessel filters with cutoff frequencies of 500 kHz, 1 MHz, 2.5 MHz, and 5 MHz, and the same data processed with eight-level wavelet denoising using LDT and garrote thresholding. The numbers in the legend indicate the baseline noise level, as calculated from the standard deviation of the time trace over an event-free 1 ms window. In these measured data in which both white and f^2 noise contaminate the signal of interest, wavelet denoising performs remarkably well, offering lower noise than that achieved even with a 500 kHz Bessel filter, reducing noise by approximately 12 dB compared to the 2.5 MHz Bessel filter. The 2.5 MHz Bessel filtered output most closely matches the

temporal characteristics preserved by wavelet denoising, as shown by the trace of a single event in Figure 3b and the amplitude versus dwell-time histogram in Figure 3c.

We also applied this denoising technique to data obtained from high-bandwidth ion-channel recordings of the Type 1 ryanodine receptor (RyR1) using the same CMOS-integrated amplifiers³⁰ (Figure 4a). RyR1 is a Ca^{2+} -induced Ca^{2+} release channel that is found on the sarcoplasmic reticulum in skeletal muscle. The data shown here were recorded at 200-mV bias applied across a single RyR1 channel incorporated in a suspended lipid bilayer immersed in a solution containing 1 mM of adenosine triphosphate (ATP) and 40 μM of unbound Ca^{2+} (see the Supporting Information for details). The signals were obtained using the same 40 MSPS acquisition system, filtered using a 1 MHz fourth-order Bessel filter and down-sampled to 4 MSPS. Figure 4b shows a 1 s time trace comparing the outputs of fourth-order Bessel filters with cutoff frequencies of 25, 100, and 250 kHz with seven-level wavelet denoising using hard thresholding. We extract the thresholds used for wavelet denoising from the wavelet transform of pure-noise data recorded before the start of the actual experiment. The upward spikes (see the Supporting Information for details) visible in the wavelet-denoised time trace are an artifact of the hard thresholding scheme and are easily discarded because of their nonphysical nature. The expanded traces shown in Figure 4b indicate that the wavelet-denoised data retain temporal features better than those seen in the 100 kHz Bessel filtered data. The 25 kHz filter, on the other hand, significantly attenuates the amplitude of short-lived events. The all-points amplitude histogram in Figure 4c reveals two key findings. First, wavelet denoising offers noise performance comparable to that of the 25 kHz filter as shown by the width of the peak near the open channel current. Second, wavelet denoising preserves intermediate states in the histogram that are rendered invisible by the surrounding noise in the 100 kHz filtered data. The fact that the same peaks show up in the histogram for the 25 kHz filtered data confirms that these features are real and not an artifact of the wavelet denoising process.

Many ion channels including RyR1 have been implicated in major human diseases including heart failure,⁵⁹ sudden cardiac death,⁶⁰ and muscular dystrophy.⁶¹ Combined with recently achieved high-resolution cryogenic electron microscopic structures,^{62,63} improved SNR recordings hold the promise to provide important insights concerning ion-channel regulation and mechanisms of dysfunction linked to human diseases that may lead to new therapies. Greater edge sharpness in nanopore recordings will particularly help in analyte-detection experiments in which the accurate estimation of the dwell time is necessary.^{64,65}

In this work, we have applied wavelet-denoising techniques to improve SNR in nanopore and ion-channel recordings. These improvements are achieved without sacrificing edge sharpness in temporal signal characteristics. Consequently, wavelet denoising can offer better SNR than the optimal Bessel filter² for a given pulse width. Combined with optimized measurement electronics to extend measurement bandwidth, this technique can enable high-fidelity and high-bandwidth analyses of conductance data characterized by pulse-like signals.

■ ASSOCIATED CONTENT

● Supporting Information

The Supporting Information is available free of charge on the ACS Publications website at DOI: 10.1021/acs.nanolett.8b04388.

Additional information on the choice of wavelet basis and thresholding scheme, the effect of different thresholding schemes, the analysis and synthesis filters, simulation details, and experimental methods (PDF)

■ AUTHOR INFORMATION

Corresponding Author

*E-mail: shepard@ee.columbia.edu.

ORCID

Siddharth Shekar: 0000-0002-9466-1402

Marija Drndic: 0000-0002-8104-2231

Funding

This work was supported in part by a grant from the W. M. Keck Foundation, by the National Institutes of Health under Grant R01HG009189, and by the National Science Foundation under Grant EFRI-1542707. Some fabrication work was performed at the University of Pennsylvania's Singh Center for Nanotechnology, an NNCI member supported by NSF Grant ECCS-1542153. M.D. and C.-C.C. also acknowledge use of TEM facilities and instrumentation supported by the NSF through the University of Pennsylvania Materials Research Science and Engineering Center (DMR-1720530).

Notes

The authors declare the following competing financial interest(s): M.D. is a founder and consultant of Goeppert, a manufacturer of nanotechnology-related products including solid-state nanopore chips, fluid cells, and TEM supplies. A.M. is a consultant and member of the board and chair of the scientific advisory board of ARMGO Pharma and owns shares in the company that is targeting RyR channels for therapeutic purposes.

■ REFERENCES

- (1) Hille, B. *Ionic Channels of Excitable Membranes*, 1st ed.; Sinauer Associates Inc.: Sunderland, MA, 1984.
- (2) Sakmann, B.; Neher, E. *Single Channel Recording*, 2nd ed.; Springer: New York, NY, 1995.
- (3) Wanunu, M. Nanopores: A Journey towards DNA Sequencing. *Phys. Life Rev.* **2012**, 9 (2), 125–158.
- (4) Li, J.; Stein, D.; McMullan, C.; Branton, D.; Aziz, M. J.; Golovchenko, J. A. Ion-Beam Sculpting at Nanometre Length Scales. *Nature* **2001**, 412 (6843), 166–169.
- (5) Bezrukov, S. M.; Kasianowicz, J. J. Current Noise Reveals Protonation Kinetics and Number of Ionizable Sites in an Open Protein Ion Channel. *Phys. Rev. Lett.* **1993**, 70, 2352.
- (6) Lu, B.; Albertorio, F.; Hoogerheide, D. P.; Golovchenko, J. A. Origins and Consequences of Velocity Fluctuations during DNA Passage through a Nanopore. *Biophys. J.* **2011**, 101 (1), 70–79.
- (7) Plesa, C.; van Loo, N.; Ketterer, P.; Dietz, H.; Dekker, C. Velocity of DNA during Translocation through a Solid-State Nanopore. *Nano Lett.* **2015**, 15 (1), 732–737.
- (8) Keyser, U. F.; Koeleman, B. N.; Van Dorp, S.; Krapf, D.; Smeets, R. M. M.; Lema, S. G.; Dekker, N. H.; Dekker, C. Direct Force Measurements on DNA in a Solid-State Nanopore. *Nat. Phys.* **2006**, 2 (7), 473–477.
- (9) Kowalczyk, S. W.; Wells, D. B.; Aksimentiev, A.; Dekker, C. Slowing down DNA Translocation through a Nanopore in Lithium Chloride. *Nano Lett.* **2012**, 12 (2), 1038–1044.

- (10) Kasianowicz, J. J.; Brandin, E.; Branton, D.; Deamer, D. W. Characterization of Individual Polynucleotide Molecules Using a Membrane Channel. *Proc. Natl. Acad. Sci. U. S. A.* **1996**, *93* (24), 13770–13773.
- (11) Waduge, P.; Hu, R.; Bandarkar, P.; Yamazaki, H.; Cressiot, B.; Zhao, Q.; Whitford, P. C.; Wanunu, M. Nanopore-Based Measurements of Protein Size, Fluctuations, and Conformational Changes. *ACS Nano* **2017**, *11*, 5706.
- (12) Henley, R. Y.; Carson, S.; Wanunu, M. *Studies of RNA Sequence and Structure Using Nanopores*; Elsevier Inc.: Amsterdam, The Netherlands, 2016; Vol. 139.
- (13) Niedzwiecki, D. J.; Lanci, C. J.; Shemer, G.; Cheng, P. S.; Saven, J. G.; Drndić, M. Observing Changes in the Structure and Oligomerization State of a Helical Protein Dimer Using Solid-State Nanopores. *ACS Nano* **2015**, *9* (9), 8907–8915.
- (14) Gilbert, S. M.; Dunn, G.; Azizi, A.; Pham, T.; Shevitski, B.; Dimitrov, E.; Liu, S.; Aloni, S.; Zettl, A. Fabrication of Subnanometer-Precision Nanopores in Hexagonal Boron Nitride. *Sci. Rep.* **2017**, *7* (1), 4–8.
- (15) Venta, K.; Shemer, G.; Puster, M.; Rodríguez-Manzo, J. A.; Balan, A.; Rosenstein, J. K.; Shepard, K.; Drndić, M. Differentiation of Short, Single-Stranded DNA Homopolymers in Solid-State Nanopores. *ACS Nano* **2013**, *7* (5), 4629–4636.
- (16) Rodríguez-Manzo, J. A.; Puster, M.; Nicolai, A.; Meunier, V.; Drndić, M. DNA Translocation in Nanometer Thick Silicon Nanopores. *ACS Nano* **2015**, *9* (6), 6555–6564.
- (17) Deamer, D. W.; Akeson, M.; Branton, D. Three Decades of Nanopore Sequencing. *Nat. Biotechnol.* **2016**, *34* (5), 518–524.
- (18) Larkin, J.; Henley, R. Y.; Muthukumar, M.; Rosenstein, J. K.; Wanunu, M. High-Bandwidth Protein Analysis Using Solid-State Nanopores. *Biophys. J.* **2014**, *106* (3), 696–704.
- (19) Shekar, S.; Niedzwiecki, D. J.; Chien, C.-C.; Ong, P.; Fleischer, D. A.; Lin, J.; Rosenstein, J. K.; Drndić, M.; Shepard, K. L. Measurement of DNA Translocation Dynamics in a Solid-State Nanopore at 100 ns Temporal Resolution. *Nano Lett.* **2016**, *16* (7), 4483–4489.
- (20) Rosenstein, J. K.; Ramakrishnan, S.; Roseman, J.; Shepard, K. L. Single Ion Channel Recordings with CMOS-Anchored Lipid Membranes. *Nano Lett.* **2013**, *13* (6), 2682–2686.
- (21) Tabard-Cossa, V.; Trivedi, D.; Wiggan, M.; Jetha, N. N.; Marziali, A. Noise Analysis and Reduction in Solid-State Nanopores. *Nanotechnology* **2007**, *18*, 305505.
- (22) Smeets, R. M. M.; Dekker, N. H.; Dekker, C. Low-Frequency Noise in Solid-State Nanopores. *Nanotechnology* **2009**, *20* (9), 095501.
- (23) Läuger, P. Shot Noise in Ion Channels. *Biochim. Biophys. Acta, Biomembr.* **1975**, *413* (1), 1–10.
- (24) Rosenstein, J. K.; Shepard, K. L. Temporal Resolution of Nanopore Sensor Recordings. *Proc. Annu. Int. Conf. IEEE Eng. Med. Biol. Soc. EMBS* **2013**, 4110–4113.
- (25) Crescentini, M.; Bennati, M.; Carminati, M.; Tartagni, M. Noise Limits of CMOS Current Interfaces for Biosensors: A Review. *IEEE Trans. Biomed. Circuits Syst.* **2014**, *8* (2), 278–292.
- (26) Ciccarella, P.; Carminati, M.; Ferrari, G.; Fraccari, R. L.; Bahrami, A. Integrated Low-Noise Current Amplifier for Glass-Based Nanopore Sensing, Proceedings 10th Conference on Ph.D. Research in Microelectronics and Electronics (PRIME), Grenoble, France, June 30–July 3; 2014; pp 1–4.
- (27) Crescentini, M.; Thei, F.; Bennati, M.; Saha, S.; De Planque, M. R. R.; Morgan, H.; Tartagni, M. A Distributed Amplifier System for Bilayer Lipid Membrane (BLM) Arrays with Noise and Individual Offset Cancellation. *IEEE Trans. Biomed. Circuits Syst.* **2015**, *9* (3), 334–344.
- (28) Weerakoon, P.; Klemic, K.; Sigworth, F. J.; Culurciello, E. An Integrated Patch-Clamp Amplifier for High-Density Whole-Cell Recordings. *2007 IEEE Int. Symp. Circuits Syst.* **2007**, 1205–1208.
- (29) Rosenstein, J. K.; Wanunu, M.; Merchant, C.; Drndić, M.; Shepard, K. L. Integrated Nanopore Sensing Platform with Sub-Microsecond Temporal Resolution. *Nat. Methods* **2012**, *9* (5), 487–492.
- (30) Hartel, A. J. W.; Ong, P.; Schroeder, I.; Giese, M. H.; Shekar, S.; Clarke, O. B.; Zalk, R.; Marks, A. R.; Hendrickson, W. A.; Shepard, K. L. Single-Channel Recordings of RyR1 at Microsecond Resolution in CMOS-Suspended Membranes. *Proc. Natl. Acad. Sci. U. S. A.* **2018**, *115* (8), E1789–E1798.
- (31) Colquhoun, D.; Sigworth, F. J. Fitting and Statistical Analysis of Single Channel Records. *Single Channel Rec* **1995**, 483.
- (32) Timp, W.; Comer, J.; Aksimentiev, A. DNA Base-Calling from a Nanopore Using a Viterbi Algorithm. *Biophys. J.* **2012**, *102* (10), L37.
- (33) Emmett, K. J.; Rosenstein, J. K.; van de Meent, J.-W.; Shepard, K. L.; Wiggins, C. H. Statistical Inference for Nanopore Sequencing with a Biased Random Walk Model. *Biophys. J.* **2015**, *108* (8), 1852–1855.
- (34) Venkataramanan, L.; Sigworth, F. J. Applying Hidden Markov Models to the Analysis of Single Ion Channel Activity. *Biophys. J.* **2002**, *82* (4), 1930–1942.
- (35) Venkataramanan, L.; Walsh, J. L.; Kuc, R.; Sigworth, F. J. Identification of Hidden Markov Models for Ion Channel Currents-Part I: Colored Background Noise. *IEEE Trans. Signal Process.* **1998**, *46* (7), 1901–1915.
- (36) Qin, F. Restoration of Single-Channel Currents Using the Segmental k-Means Method Based on Hidden Markov Modeling. *Biophys. J.* **2004**, *86* (3), 1488–1501.
- (37) Ivanov, P. C.; Rosenblum, M. G.; Peng, C. K.; Mietus, J.; Havlin, S.; Stanley, H. E.; Goldberger, A. L. Scaling Behaviour of Heartbeat Intervals Obtained by Wavelet-Based Time-Series Analysis. *Nature* **1996**, *383*, 323–327.
- (38) Chaovalit, P.; Gangopadhyay, A.; Karabatis, G.; Chen, Z. Discrete Wavelet Transform-Based Time Series Analysis and Mining. *ACM Comput. Surv.* **2011**, *43* (2), 1–37.
- (39) Torrence, C.; Compo, G. P. A Practical Guide to Wavelet Analysis. *Bull. Am. Meteorol. Soc.* **1998**, *79* (1), 61–78.
- (40) Percival, D. B.; Walden, A. T. Introduction to Wavelets. In *Wavelet Methods for Time Series Analysis*; Cambridge University Press: Cambridge, U.K., 2000.
- (41) Bullmore, E.; Long, C.; Suckling, J.; Fadili, J.; Calvert, G.; Zelaya, F.; Carpenter, T. A.; Brammer, M. Colored Noise and Computational Inference in FMRI Time Series Analysis: Resampling Methods in Time and Wavelet Domains SInstitute of Psychiatry KCL, London UK. *NeuroImage* **2001**, *13* (6), 86.
- (42) Hosein-Sooklal, A.; Kargol, A. Wavelet Analysis of Non-equilibrium Ionic Currents in Human Heart Sodium Channel (HH1a). *J. Membr. Biol.* **2002**, *188* (3), 199–212.
- (43) Jagtiani, A. V.; Sawant, R.; Carletta, J.; Zhe, J. Wavelet Transform-Based Methods for Denoising of Coulter Counter Signals. *Meas. Sci. Technol.* **2008**, *19* (6), 065102.
- (44) Arjmandi, N.; Van Roy, W.; Lagae, L.; Borghs, G. Improved Algorithms for Nanopore Signal Processing. *Nanopores for Bioanalytical Applications: Proceedings of the International Conference* **2012**, 11–17.
- (45) Mallat, S. G. A. Theory for Multiresolution Signal Decomposition: The Wavelet Representation. *IEEE Trans. Pattern Anal. Mach. Intell.* **1989**, *11* (7), 674–693.
- (46) Cohen, A.; Daubechies, I.; Feauveau, J.-C. Biorthogonal Bases of Symmetric Compactly Supported Wavelets. *Commun. Pure Appl. Math.* **1992**, *45*, 485–560.
- (47) Vetterli, M.; Herley, C. Wavelets and Filter Banks: Theory and Design. *IEEE Trans. Signal Process.* **1992**, *40* (9), 2207–2232.
- (48) Strang, G. Wavelet Transforms versus Fourier Transforms. *Bull. Am. Math. Soc.* **1993**, *28* (2), 288–305.
- (49) Coifman, R. R.; Donoho, D. L. *Translation-Invariant De-Noising*; Antoniadis, A., Oppenheim, G., Eds.; Springer, New York, NY, 1995; Vol. 103.
- (50) Donoho, D. L.; Johnstone, I. M. Ideal Spatial Adaptation by Wavelet Shrinkage. *Biometrika* **1994**, *81*, 425–455.
- (51) Johnstone, I. M.; Silverman, B. W. Wavelet Threshold Estimators for Data with Correlated Noise. *J. R. Stat. Soc. Ser. B (Statistical Methodol.)* **1997**, *59* (2), 319–351.
- (52) Donoho, D. L.; Johnstone, I. M. Adapting to Unknown Smoothness via Wavelet Shrinkage. *J. Am. Stat. Assoc.* **1995**, *90* (432), 1200–1224.

- (53) Chang, S. G.; Yu, B.; Vetterli, M. Adaptive Wavelet Thresholding for Image Denoising and Compression. *IEEE Trans. Image Process.* **2000**, *9* (9), 1532–1546.
- (54) Gao, H.-Y.; Bruce, A. G. WaveShrink with Firm Shrinkage. *Stat. Sin.* **1997**, *7*, 855–874.
- (55) Gao, H.-Y. Wavelet Shrinkage Denoising Using the Non-Negative Garrote. *J. Comput. Graph. Stat.* **1998**, *7* (4), 469–488.
- (56) Ogden, T.; Parzen, E. Data Dependent Wavelet Thresholding in Nonparametric Regression with Change-Point Applications. *Comput. Stat. Data Anal.* **1996**, *22* (1), 53–70.
- (57) Srivastava, M.; Anderson, C. L.; Freed, J. H. A New Wavelet Denoising Method for Selecting Decomposition Levels and Noise Thresholds. *IEEE Access* **2016**, *4*, 3862–3877.
- (58) Balan, A.; Chien, C. C.; Engelke, R.; Drndic, M. Suspended Solid-State Membranes on Glass Chips with Sub 1-PF Capacitance for Biomolecule Sensing Applications. *Sci. Rep.* **2016**, *5* (1), 17775.
- (59) Marx, S. O.; Reiken, S.; Hisamatsu, Y.; Jayaraman, T.; Burkhoff, D.; Rosembliit, N.; Marks, A. R. PKA Phosphorylation Dissociates FKBP12.6 from the Calcium Release Channel (Ryanodine Receptor): Defective Regulation in Failing Hearts. *Cell* **2000**, *101* (4), 365–376.
- (60) Wehrens, X. H. T.; Lehnart, S. E.; Huang, F.; Vest, J. A.; Reiken, S. R.; Mohler, P. J.; Sun, J.; Guatimosim, S.; Song, L. S.; Rosembliit, N.; et al. FKBP12.6 Deficiency and Defective Calcium Release Channel (Ryanodine Receptor) Function Linked to Exercise-Induced Sudden Cardiac Death. *Cell* **2003**, *113* (7), 829–840.
- (61) Bellinger, A. M.; Reiken, S.; Carlson, C.; Mongillo, M.; Liu, X.; Rothman, L.; Matecki, S.; Lacampagne, A.; Marks, A. R. Hyper-nitrosylated Ryanodine Receptor Calcium Release Channels Are Leaky in Dystrophic Muscle. *Nat. Med.* **2009**, *15* (3), 325–330.
- (62) Zalk, R.; Clarke, O. B.; des Georges, A.; Grassucci, R. A.; Reiken, S.; Mancina, F.; Hendrickson, W. A.; Frank, J.; Marks, A. R. Structure of a Mammalian Ryanodine Receptor. *Nature* **2015**, *517* (7532), 44–49.
- (63) des Georges, A.; Clarke, O. B.; Zalk, R.; Yuan, Q.; Condon, K. J.; Grassucci, R. A.; Hendrickson, W. A.; Marks, A. R.; Frank, J. Structural Basis for Gating and Activation of RyR1. *Cell* **2016**, *167* (1), 145–157.
- (64) Kasianowicz, J. J.; Robertson, J. W. F.; Chan, E. R.; Reiner, J. E.; Stanford, V. M. Nanoscopic Porous Sensors. *Annu. Rev. Anal. Chem.* **2008**, *1* (1), 737–766.
- (65) Balijepalli, A.; Ettegui, J.; Cornio, A. T.; Robertson, J. W. F.; Cheung, K. P.; Kasianowicz, J. J.; Vaz, C. Quantifying Short-Lived Events in Multistate Ionic Current Measurements. *ACS Nano* **2014**, *8* (2), 1547–1553.